### Title

The role of the CeO 2 /BiVO 4 interface in optimized Fe–Ce oxide coatings for solar fuels photoanodes




### Journal

Journal of Materials Chemistry A, 4(37)

### ISSN

2050-7488



### Authors

Shinde, A
Li, G
Zhou, L
et al.



### Publication Date

2016

### DOI

10.1039/c6ta04746g

Peer reviewed

Journal of Materials Chemistry A

PAPER

View Article Online
View Journal | View Issue



Cite this: J. Mater. Chem. A, 2016, 4, 14356

# The role of the $CeO_2$/$BiVO_4$ interface in optimized Fe–Ce oxide coatings for solar fuels photoanodes†

A. Shinde,‡[a] G. Li,‡[b] L. Zhou,‡[a] D. Guevarra,[a] S. K. Suram,[a] F. M. Toma,[bc] Q. Yan,[de] J. A. Haber,*[a] J. B. Neaton*[bdef] and J. M. Gregoire*[a]

Received 6th June 2016
Accepted 26th August 2016

DOI: 10.1039/c6ta04746g

www.rsc.org/MaterialsA

Solar fuel generators entail a high degree of materials integration, and efficient photoelectrocatalysis of the constituent reactions hinges upon the establishment of highly functional interfaces. The recent application of high throughput experimentation to interface discovery for solar fuels photoanodes has revealed several surprising and promising mixed-metal oxide coatings for $BiVO_4$. Using sputter deposition of composition and thickness gradients on a uniform $BiVO_4$ film, we systematically explore photoanodic performance as a function of the composition and loading of Fe–Ce oxide coatings. This combinatorial materials integration study not only enhances the performance of this new class of materials but also identifies $CeO_2$ as a critical ingredient that merits detailed study. A heteroepitaxial $CeO_2$(001)/$BiVO_4$(010) interface is identified in which Bi and V remain fully coordinated to O such that no surface states are formed. *Ab initio* calculations of the integrated materials and inspection of the electronic structure reveals mechanisms by which $CeO_2$ facilitates charge transport while mitigating deleterious recombination. The results support the observations that addition of Ce to $BiVO_4$ coatings greatly enhances photoelectrocatalytic activity, providing an important strategy for developing a scalable solar fuels technology.

## Introduction

Solar-driven photoelectrochemical (PEC) synthesis of $H_2$ or C-containing fuels is a promising technology for generating storable and sustainable transportation fuels. Water is widely accepted as the only scalable proton and electron source for fuel synthesis reactions, making photoelectrocatalysis of the oxygen evolution reaction (OER) a critical component of solar fuels technology.[1] The use of semiconductor/liquid junctions for separating photo-excited charges to drive the OER is particularly attractive for its simplicity and potential for low cost relative to solid state photovoltaic (PV) junctions.[2] To obtain such a photoanode system, an n-type metal oxide semiconductor is typically employed, as oxide-based semiconductors provide the best opportunity for performing the anodic OER reaction without semiconductor degradation in the highly-oxidizing electrochemical environment.[3] Materials requirements for efficient OER photocatalysis include a band gap energy in the visible range and application of surface coatings that serve a variety of functions, including modification of the semiconductor surface to promote catalytic acceleration of OER kinetics.[2,4] Monoclinic $BiVO_4$ has emerged as the prevalent metal oxide semiconductor for solar fuels photoanodes despite inherent issues with a slightly too-large gap near 2.5 eV and insufficient stability under operational conditions.[5,6] $BiVO_4$-based photoanodes[7] still offer great promise for enabling efficient, scalable solar fuel generators,[8,9] particularly if optimal surface coatings can be identified. Indeed, the present work indicates that $BiVO_4$ does not form a very effective semiconductor–liquid junction due to sensitivity of the electronic structure to surface defects, and we demonstrate that judicious application of a metal oxide coating can preserve the electronic structure to yield effective semiconductor–coating–liquid junctions.

Since metal oxides can be readily screened for OER electrocatalysis,[10,11] identifying coatings that serve the desired catalytic function is somewhat straightforward but is insufficient for predicting the performance of integrated photoanodes due to the importance of properties that are particular to the coating/semiconductor interface.[12] For example, $IrO_x$ is a prolific OER catalyst but is relatively ineffective at enhancing PEC performance when applied to $BiVO_4$.[13,14] Libraries of coatings on

[a]Joint Center for Artificial Photosynthesis, California Institute of Technology, Pasadena, CA 91125, USA. E-mail: jahaber@caltech.edu; gregoire@caltech.edu
[b]Joint Center for Artificial Photosynthesis, Lawrence Berkeley National Laboratory, Berkeley, CA 94720, USA. E-mail: jbneaton@lbl.gov
[c]Chemical Sciences Division, Lawrence Berkeley National Laboratory, Berkeley, CA 94720, USA
[d]Molecular Foundry, Lawrence Berkeley National Laboratory, Berkeley, CA 94720, USA
[e]Department of Physics, University of California, Berkeley, Berkeley, CA 94720, USA
[f]Kavli Energy NanoSciences Institute, University of California, Berkeley, Berkeley, CA 94720, USA

† Electronic supplementary information (ESI) available. See DOI: 10.1039/c6ta04746g

‡ Equal contribution.

$BiVO_4$ with 4 (ref. 14) and 13 (ref. 15) different compositions have been prepared by pipetting metal oxide precursors and we scaled this general strategy using inkjet (IJ) printing to deposit hundreds of catalyst compositions on a $BiVO_4$-coated plate.[16,17] We also synthesized 3 different loadings of each catalyst composition and in total performed a suite of electrochemical, optical, and photoelectrochemical measurements on 1716 metal oxide coatings in the (Ni–La–Co–Ce)$O_x$ (ref. 16) and (Ni–Fe–Co–Ce)$O_x$ (ref. 17) composition spaces in pH 13 electrolyte.

The statistical analysis of these large datasets demonstrates that PEC performance is not strongly correlated with either catalytic or optical properties of the metal oxide coatings, demonstrating that while optical transmission of coatings is important for front-side-illuminated photoanodes, the primary role of a metal oxide coating on $BiVO_4$ is mitigation of non-catalytic recombination. High throughput screening revealed several surprising high-performance photoanodes in which specific ternary, quaternary, and quinary metal oxide compositions appear to form excellent interfaces with $BiVO_4$. The most common feature of these optimal metal oxide coatings is a Ce concentration between 40% and 90% of the metal species. In particular, (Fe–Ce)$O_x$ coatings with 40–60% Ce were found to provide the best PEC performance with the fewest number of elements in the coating.

FeOOH coatings have been demonstrated to greatly enhance PEC properties of $BiVO_4$ in near-neutral pH electrolytes,[13,18,19] and while the Fe-based coating in the high throughput study did exhibit improved PEC performance in pH 13, the addition of Ce to form a mixed-metal oxide coating greatly enhanced performance. The PEC performance of (Fe–Ce)$O_x$/$BiVO_4$ photoanodes increased with decreased Fe–Ce loading, although the range of loading available for exploration and the control of the coating morphology was practically limited by the IJ deposition technique. To further explore the PEC performance as a function of composition, we employ combinatorial physical vapor deposition (PVD) in the present work, which is a scalable coating technique that provides systematic exploration of the parameter space with a much more conformal coating than that provided by the previously-reported combinatorial techniques.

The results confirm the enhancement in $BiVO_4$ PEC performance with these coatings and additionally reveal that coatings with up to 90% Ce are near-optimal. The more-uniform morphology of the PVD coatings and the use of continuous, gradual gradients in coating composition and loading clearly demonstrate the efficacy of thin, Ce-rich coatings, creating further intrigue regarding how $CeO_2$ interfaces with $BiVO_4$. While operational interfaces are notoriously difficult to model,[20] important insights into the control of surface electronic structure are provided with computational modelling of heteroepitaxial $CeO_2$/$BiVO_4$ interfaces. We find that $CeO_2$ coatings can prevent the formation of mid-gap trap states and provide hole transport to catalytic sites, all while maintaining the desirable optical transparency of photoanode coatings. Since $BiVO_4$ contains electronically active defect states that lead to significant photo-carrier recombination losses,[21] our results suggest that the inclusion of $CeO_2$ in mixed-metal oxide or multi-layer[22] coatings will help address a primary performance-limiting issue with this important solar fuels material.

## Experimental and computational

### Experimental

A uniform, spin-coated, $BiVO_4$ light absorber thin film was deposited onto the fluorine doped tin oxide (FTO) coated side of 10 cm × 10 cm glass plates (TEC-15 Sigma Aldrich) following a literature protocol.[5,23] Solutions of bismuth(III) nitrate pentahydrate (Sigma Aldrich, ≥98%) in acetylacetone (Sigma Aldrich, ≥99%) and vanadium(IV)-oxy acetylacetonate in acetylacetone were prepared, mixed, spin-coated onto FTO coated glass plates, and annealed as previously described.[16] Phase-pure monoclinic $BiVO_4$ was verified by X-ray Diffraction (XRD) analysis.

The Fe–Ce oxide libraries were fabricated using reactive RF magnetron co-sputtering of Fe (99.95%, ACI Alloy Inc.) and Ce (99.95%, ACI Alloy Inc.) metal targets at room temperature onto the $BiVO_4$-coated plates, and to measure film composition and thickness, duplicate Fe–Ce libraries were deposited onto 10 cm-diameter Si wafers with a thermal oxide diffusion barrier. All depositions proceeded in a combinatorial sputtering system (Kurt J. Lesker, CMS24) with $10^{-5}$ Pa base pressure and a deposition atmosphere composed of inert sputtering gas Ar (0.64 Pa) and reactive gas $O_2$ (0.16 Pa). The composition and thickness gradients in each co-sputtered library were attained by positioning the deposition sources in a non-confocal geometry.[24] Prior to each deposition, the Fe and Ce targets were pre-cleaned at Ar pressure of 0.80 Pa for 20 min to eliminate possible target contamination. The power applied to the Ce target was 70 W for all depositions, and both the power applied to the Fe target and the deposition time were varied to attain the desired composition and thickness as follows: 150 W, 35 min for library A; 70 W, 30 min for library B; and 33 W, 13 min for library C.

X-ray fluorescence (XRF) spectroscopy was employed to map the Fe and Ce content of the libraries deposited on Si; further details of which can be found in the ESI.† The morphologies of the selected high performance compositions were studied using SEM performed on a FEI Nova NanoSEM 450 and AFM performed on a Bruker Dimension Icon operating in ScanAsyst mode with Bruker ScanAsyst-Air probes. The AFM images were analyzed using NanoScope Analyst software (version 1.40).

Photoelectrochemical experiments were performed in aqueous 0.1 M sodium hydroxide with 0.5 M sodium sulfate as a supporting electrolyte (pH 13) using a xenon arc lamp and scanning drop electrochemical cell (SDC), as described previously.[16] The illumination irradiance exceeds that of AM 1.5, particularly in the ultraviolet range, and the spectrum is provided in the ESI.† Toggled-illumination cyclic voltammetry (CV) measurements were performed on the Fe–Ce libraries with a potential sweep from 1.23 to 0.585 V and back to 1.23 V *vs.* RHE (0 to −0.645 V and back to 0 V *vs.* the $O_2$/$H_2O$ Nernstian potential) at a scan rate of 0.02 V $s^{-1}$. Illumination was toggled at 0.5 Hz (1.34 s on, 0.67 s off) during the CV. The SDC was rastered along each 10 cm × 10 cm library plate with CV measurements acquired on a 5 mm square grid, and avoiding

visually-apparent non-uniformities on the perimeter of the plate resulted in 300–340 samples per library plate. Automated CV data analysis was performed as described previously,[16] in which current transients upon illumination toggling were disregarded and the remaining illuminated and dark current signals of the anodic sweep of each CV were used to construct the photocurrent density ($J$) – potential ($V$) signal. Under the assumption of 100% faradaic efficiency for the OER, the electrochemical power generation (or power saved[25] compared to an electrocatalyst operating at the Nernstian potential) was calculated as the product of the reverse bias potential (1.23 V *vs.* RHE – $V$) and the corresponding photocurrent.

### Computational

Spin-polarized density functional theory (DFT) calculations were performed on $BiVO_4$, $CeO_2$, and heterostructures of these oxides using VASP.[26,27] The lattice parameters of bulk $BiVO_4$ and $CeO_2$ crystals, in monoclinic ($C2/c$) and fluorite ($Fm\bar{3}m$) room-temperature phases, respectively, were optimized with DFT within the generalized gradient approximation (GGA) of Perdew, Ernzehof, and Burke (PBE).[28,29] On-site Ce f-electron exchange and correlation effects were further treated with a Hubbard $U$ correction,[30,31] applied in a rotationally-invariant, basis-set-independent formalism.[32,33] The DFT-PBE and DFT-PBE+U calculations used a plane-wave basis and projector augmented-wave (PAW) potentials,[34,35] requiring a plane-wave cutoff of 520 eV. All the structures were fully relaxed until the forces on each atom were less than 0.01 eV $Å^{-1}$. A Hubbard $U$ of 5 eV, used in prior DFT-PBE+U work on Ce,[36] was adopted for structural optimizations.

Electronic structure calculations of $BiVO_4$, $CeO_2$, and their heterostructures were performed using $k$-meshes of 3 × 2 × 5, 4 × 4 × 4, and 3 × 3 × 1, respectively. For calculating the projected density of states (PDOS) and band structure, a large Hubbard $U$ of 12 eV was used for the Ce f states to establish agreement between the calculated and experimental $CeO_2$ band gap values. In the supercell calculations of heterostructures, dipole corrections[37,38] were used to remove spurious effects of the periodic boundary conditions.

## Results and discussion

### Combinatorial materials integration

Motivated by the recent discovery that inkjet-printed $Fe_xCe_{1-x}O_z$ coatings form excellent interfaces with thin film $BiVO_4$,[17] a library of such coatings was prepared by PVD using reactive co-sputtering with no heating other than that from the sputtering ambient. The study of IJ libraries identified $x$ = 0.3 to 0.7 with metal loading ($L$) between 0.75 and 3.8 nmol $mm^{-2}$ as excellent coatings for $BiVO_4$, and the PVD library was prepared to cover much of this composition and loading range on a single 10 × 10 cm plate. We note that due to the non-planar morphology of the coatings and uncharacterized density and oxygen stoichiometry of the coating materials, we characterize the amount of coating as the molar loading of metal species measured by XRF and describe specific assumptions when a coating thickness is estimated.

The continuous PVD, $x$–$L$ gradient library was characterized by acquiring toggled-illumination CVs on a regular grid of positions noted in Fig. 1. The primary performance metric extracted from each CV was the electrochemical power generation ($P_{max}$), which is the product of the reverse bias potential and the corresponding photocurrent, also referred to as the power saved[25] compared to an electrocatalyst operating at the Nernstian potential. In Fig. 1, $P_{max}$ is mapped over both the library position space (a) and the $x$–$L$ space (b), revealing a systematic trend with respect to composition and loading.

The thin-film $BiVO_4$ for the previous IJ study and the present PVD study were prepared in the same batch synthesis and are thus nominally identical, enabling the direct comparison of optimal coatings from these different libraries. The best photoanode in the library is found at $x$ = 0.26, $L$ = 0.96 nmol $mm^{-2}$ and has a $P_{max}$ of approximately 1 mW $cm^{-2}$, substantially larger than the 0.76 mW $cm^{-2}$ obtained in the IJ library with $x$ = 0.6, $L$ = 0.75 nmol $mm^{-2}$. Fig. 2 shows the anodic sweep from toggled-illumination CVs acquired on bare $BiVO_4$ and photoanodes with the optimal IJ and PVD coatings. The photoactivity of the IJ and PVD coatings appear qualitatively similar with notable differences including the enhanced photocurrent of the

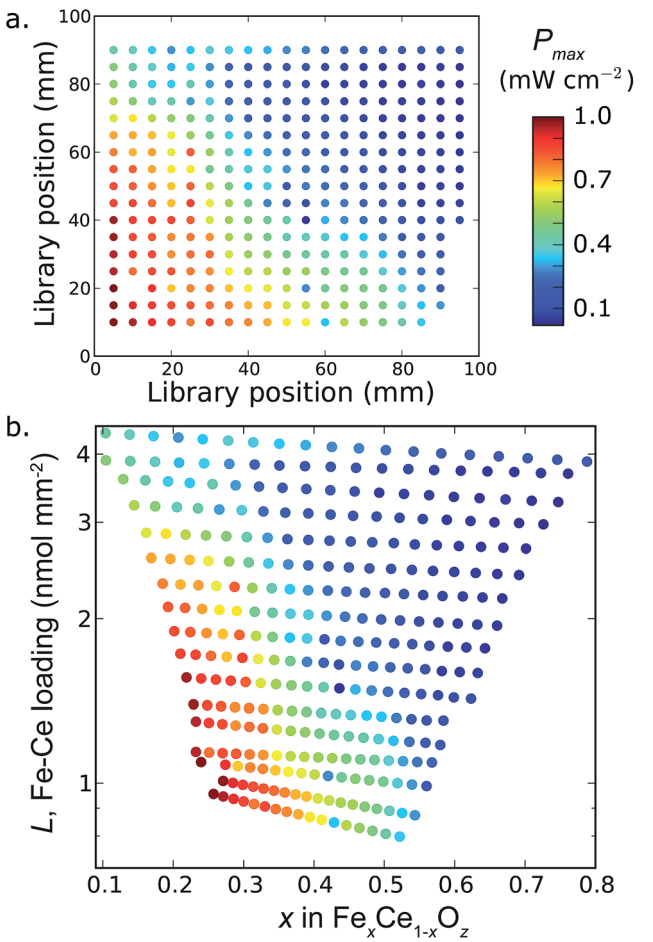


Fig. 1 The $P_{max}$ values from Fe–Ce coatings in PVD library A mapped using the library positions (a) and the catalyst composition and loading (b).

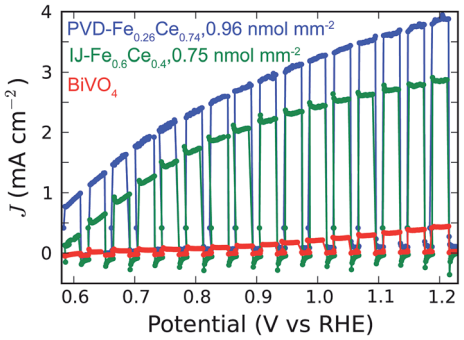


Fig. 2 Toggled-illumination anodic voltage sweep (0.02 V $s^{-1}$) for the Fe–Ce coating with highest $P_{max}$ in PVD library A in the present work, the IJ library from previous work, and bare $BiVO_4$.

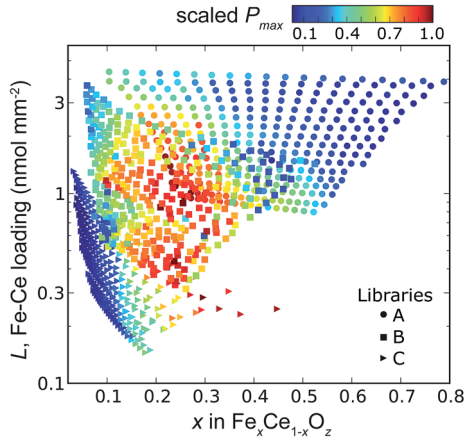


Fig. 3 The composition-loading map of $P_{max}$ for 3 Fe–Ce coating libraries. The $P_{max}$ for each sample was scaled by the maximum value for the respective library to mitigate the influence from library-specific $BiVO_4$ quality.

PVD sample, especially at low potential. Near 0.6 V *vs.* RHE, the photocurrent of the PVD sample is approximately twice that of the IJ sample, and concomitantly it appears that the illuminated open circuit potential of the PVD sample is much better and likely below 0.5 V *vs.* RHE. The PVD coating also appears to lower the current transient upon illumination when compared to the IJ coating, indicating improved charge carrier extraction. These CVs were performed between the Nernstian potential for the OER (1.23 V *vs.* RHE) and the approximate open circuit potential of bare $BiVO_4$, demonstrating the excellent improvement provided by the PVD $Fe_xCe_{1-x}O_z$ coating and motivating more detailed PEC characterization in future work.

The IJ coatings have a coarse morphology and are discontinuous (non-conformal), so the improved performance from a more-conformal PVD coating with optimized loading was somewhat expected. The more surprising result provided by Fig. 1 is that the maximum $P_{max}$ appears at more Ce-rich coatings with lower loading. For loadings of approximately 1 nmol $mm^{-2}$, the composition $x = 0.3$ exhibits a 2-fold improvement in $P_{max}$ compared to $x = 0.5$. To further explore thin, Ce-rich coatings, 2 additional libraries were synthesized. The 3 libraries are referred to as A, B, and C in order of decreasing metal loading, where library A is the library shown in Fig. 1. The $BiVO_4$ films prepared for libraries B and C were synthesized in separate experiments from each other and from that of Library A and additionally experienced slightly different thermal histories, resulting in different baseline photoactivities of the $BiVO_4$ and hampering comparison of absolute $P_{max}$ values among the 3 libraries. Calibrations of the native $BiVO_4$ photoactivity could not be performed due to the complete coating of the $BiVO_4$ during the PVD deposition. The maps of $P_{max}$ for libraries A, B, and C are shown in Fig. S1,† and to visualize the full $x$–$L$ map from the 3 libraries, we scale each library's $P_{max}$ values by the maximum value observed within that library. Fig. 3 contains the scaled-$P_{max}$ data for all 3 libraries, which shows that there are overlapping $x$–$L$ regions between libraries A and B and between libraries B and C. The scaled $P_{max}$ is in reasonable agreement in these regions, indicating that this figure sufficiently represents the relative $x$–$L$ variation in PEC performance across all 3 libraries.

The full $x$–$L$ map shows that the locally optimal sample from library A ($x = 0.26$, $L = 0.96$ nmol $mm^{-2}$, see Fig. 2) is among the globally best samples among the 3 libraries and that near-optimal coatings are obtained over a fairly wide $x$–$L$ region near $x = 0.26$ with loadings from 0.2 to 1.5 nmol $mm^{-2}$. Several near-edge samples from library C also suggest that equivalent performance may be obtained at more thin, Fe-rich coatings, although additional experiments are needed to more completely evaluate coatings in this range of $x$ and $L$.

To characterize the morphology of the catalyst coatings, atomic force microscopy (AFM) and scanning electron microscopy (SEM) imaging were performed on a spot from Library B that had not been exposed to electrolyte. The $x = 0.26$, $L = 0.89$ nmol $mm^{-2}$ sample lies approximately at the center of the optimal region in Fig. 3, and the AFM and SEM data is shown in Fig. 4 along with an AFM image of bare $BiVO_4$ from a separate synthesis. While the $BiVO_4$ in Fig. 4c appears to have a different characteristic particle size than that of Fig. 4a and b, the most pertinent difference is the appearance of a fine morphology from the $Fe_{0.26}Ce_{0.74}O_z$ coating. The coating appears to be quite conformal with characteristic particle size of approximately 13 nm. Using the bulk $Fe_2O_3$ and $CeO_2$ densities, the nominal thickness of this sample is 19 nm, implying that the observed particle feature size in Fig. 4a and b is approximately 70% of the

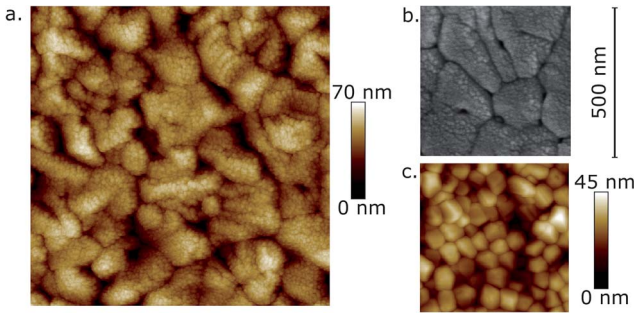


Fig. 4 Morphology of the $Fe_{0.26}Ce_{0.74}O_z$, 0.89 nmol $mm^{-2}$ coating on $BiVO_4$ from AFM (a) and SEM (b) imaging, along with an AFM image of bare $BiVO_4$ (c). The 500 nm scale bar applies to all images.

coating thickness. Initial investigation of other samples in library B indicate that the morphology of Fig. 4a and b is representative of the Fe–Ce coatings in this library. The top-tier coatings are observed down to a loading of 0.2 nmol $mm^{-2}$, corresponding to a nominal thickness of less than 5 nm, motivating exploration of ultra-thin, conformal $Fe_xCe_{1-x}O_z$ coatings provided by techniques such as atomic layer deposition. Indeed, our initial investigations indicate that photoelectrochemical deposition of such coatings yields excellent photoanode performance.[17] Conformal coatings or other protection schemes are also required to eliminate $BiVO_4$ corrosion and enable long-term photoelectrochemical stability since the instability of $BiVO_4$ has been well established (see Fig. S2†).[6]

While FeOOH coatings have been demonstrated to form excellent interfaces with $BiVO_4$,[13,18,19] the Ce-rich coatings identified in both the IJ and PVD exhibit better PEC performance (only measured in pH 13 to date). As noted in our previous study on IJ-deposited coatings, which included analysis of the optical transparency of each coating, the high performance of the thin, Ce-rich catalysts is not due solely to the high optical transparency of these coatings.[16,17] Trotochaud *et al.*[39] noted through detailed photoanode modelling that the optimal thickness for Ni, Fe, and Co-based metal oxides is below 5 nm due to the high optical absorption of these metal oxides under operating conditions. The higher optimal thickness of the Ce-rich coatings is commensurate with the excellent optical transparency of these coatings, and the diminished performance for loadings exceeding 1.4 nmol $mm^{-2}$ in Fig. 3 is most likely due to hole transport limitations rather than parasitic optical absorption. Also, direct electrolyte-$BiVO_4$ contact may be important for desirable band energetics at the semiconductor–liquid junction, although the similar performance with vastly different morphologies from the IJ and PVD deposition methods indicates that a specific morphology is not required for the beneficial interfacial effects.

A more detailed investigation into the role of Ce is motivated by the excellent performance with up to 90% Ce observed in Fig. 3 and our recent observation that coatings with 70–90% Ce form excellent interfaces with $BiVO_4$ in the La–Co–Ce system. IJ-deposited, Ce-rich mixed-metal oxides have been shown to contain $CeO_2$ nanoparticles that serve as effective co-catalysts for the dark electrocatalysts of the OER,[40] but since PEC performance is not correlated with dark OER electrocatalysis performance in our IJ studies,[16,17] the primary role of Ce appears to be formation of a desirable interface with $BiVO_4$.

## Computational interface characterization

Guided by these observations, we turn to first-principles calculations to elucidate the benefits of interfacing $CeO_2$ with $BiVO_4$. At the surface of a metal oxide photoelectrode such as $BiVO_4$, defects such as oxygen vacancies are expected;[41] these defects, along with the presence of dangling bonds associated with under-coordinated surface atoms, can introduce (non-electrochemical) recombination pathways, reducing photoelectrochemical activity. In what follows, we first identify a defect-free $CeO_2/BiVO_4$ interface. We then use DFT to compute its electronic structure, and compare it to that of a $BiVO_4$ surface with an oxygen vacancy.

The DFT-PBE and DFT-PBE+U calculations of bulk structures are summarized in Fig. 5 and result in lattice parameters for $BiVO_4$ ($a = 7.31$ Å, $b = 11.74$ Å, $c = 5.17$ Å, and $\beta = 134.99°$) and $CeO_2$ ($a = 5.50$ Å) that are in excellent agreement with experimental values[42,43] and previous studies.[36,44]

Inspection of these $BiVO_4$ and $CeO_2$ crystalline phases reveals approximate lattice matching of select low-index faces. The in-plane unit cell of fluorite $CeO_2(001)$ ($a = b = 5.50$ Å and $\alpha = 90.00°$), shown in Fig. 5b, is similar to that of monoclinic $BiVO_4(010)$ ($a = b = 5.17$ Å and $\alpha = 89.99°$), shown in Fig. 5d. In the $CeO_2(001)$ unit cell, the two Ce atoms are in the same plane and the two surface O atoms are located at the bridge sites. In the $BiVO_4(010)$ unit cell, the Bi and V atoms are also in the same plane, but the bridge O atoms are slightly closer to the V atom. This analysis indicates the possibility of a heteroepitaxial $CeO_2(001)/BiVO_4(010)$ interface with lattice mismatch of approximately 6% and with O atoms in positions at the interface that may be substantially different from that of the 2 bulk structures. An important step in the study of the $CeO_2(001)/BiVO_4(010)$ interface is to ascertain the existence of an energetically-favorable O configuration between Ce and Bi–V planes.

The model cell shown in Fig. 6a is created by matching the (001) $CeO_2$ lattice planes to that of $BiVO_4(010)$. By placing this compressed $CeO_2(001)$ monolayer atop $BiVO_4(010)$, an interface is formed with metal–O coordination numbers that match the bulk structures, circumventing the formation of surface defects. To assess the energetic viability of this interface, model cells are created with 1, 2, 3, and 4 monolayers of $CeO_2(001)$ atop the 8-monolayer $BiVO_4(010)$ slab. The two sides of this heterostructure are separated by a vacuum layer of 20 Å in the

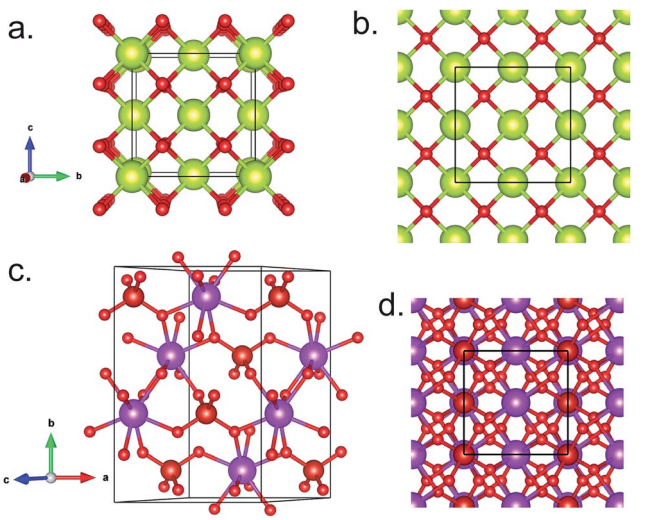


Fig. 5 Relaxed structures of (a) $CeO_2$, and (b) its (001) surface, and of (c) $BiVO_4$ and (d) its (010) surface. The Ce, Bi, and V atoms are yellow, purple, and red, respectively, with smaller red spheres representing O atoms. The surface structures in (b) and (d) are drawn with the same scale for comparison and the similar 2-D unit cells are noted in black outline.

 

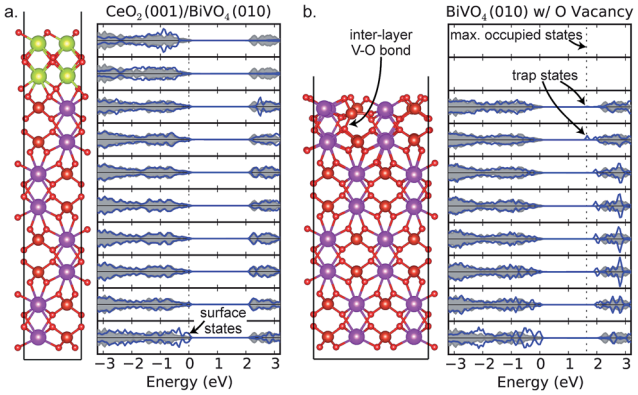


Fig. 6 The model cell and the PDOS for each monolayer for (a) $CeO_2$/$BiVO_4$ and (b) $BiVO_4$ with a surface O vacancy, where the bottom 4 layers of each cell are fixed to bulk $BiVO_4$ lattice parameters. The shaded gray in each plot is the PDOS signal for bulk $BiVO_4$. The VBM without considering trap states is set as 0 eV and the energy corresponding to the maximum occupied state is shown as a vertical dashed line in both figures.

calculation supercell with periodic boundary conditions. The bottom four monolayers of $BiVO_4$(010) are fixed to the bulk structure and the remaining 4 $BiVO_4$ and 1–4 $CeO_2$ monolayers, along with the positions of their O atoms, were allowed to vary. Fig. 6a shows the fully-relaxed supercell containing two monolayers. The formation energy associated with this arrangement is determined from its total energy ($E_{hetero}$) and the total energies of separate fully-relaxed cells as computed with DFT-PBE+U, namely the freestanding 8-monolayer $BiVO_4$ substrate ($E_{sub}$) and the freestanding $CeO_2$(001) layer(s) without the heteroepitaxy in-plane constraints ($E_{layer}$). The use of in-plane constraints in the heterostructure model leads to a higher system energy than that of a fully relaxed system, and thus the formation energy

$$E_{form} = E_{hetero} - E_{sub} - E_{layer} \quad (1)$$

provides a conservative lower bound. The $E_{form}$ values for the heterostructures with 1 to 4 monolayers of $CeO_2$ are −1.39, −1.00, −0.47, and 0.98 eV, respectively, indicating a strong driving force for the formation of the $CeO_2$(001)/$BiVO_4$(010) interface and that the energetic preference for formation of thicker $CeO_2$ layers hinges upon lattice relaxations that are not considered in these models.

To analyze the effects of the $CeO_2$ overlayers on the electronic properties of $BiVO_4$, we examine the DFT-PBE+U PDOS of each monolayer of the $CeO_2$(001)/$BiVO_4$(010) heterostructure, as shown in Fig. 6a, and compare with the corresponding PDOS for bulk $BiVO_4$. The PDOS of each $BiVO_4$ layer near the $CeO_2$ interface is nearly identical to that of bulk $BiVO_4$, demonstrating that the $CeO_2$ overlayers do not result in the formation of surface states or trap states in the $BiVO_4$. The valence band PDOS of the $CeO_2$ layer remains somewhat similar to that of bulk $BiVO_4$ with a slight shift to more negative energies. This observation suggests that with the addition of band bending due to equilibration of the metal oxide Fermi level with the OER Nernstian potential, photo-generated holes in $BiVO_4$ would experience a slight energy barrier along their energetically down-hill path to the interface with the liquid electrolyte.

To confirm that the $CeO_2$ coating provides a net benefit to the electronic structure of the $BiVO_4$ surface, we consider the PDOS for both uncoated and defective layers. The bottom $BiVO_4$ layer in Fig. 6a contains a vacuum interface, and in this O-terminated $BiVO_4$(010) surface the O coordination of Bi is 6-fold, which is lower than the 8-fold coordination in the bulk. Consequently, the PDOS of this layer deviates from bulk-like behavior, revealing the formation of surface states, especially in the valence band. The integrity of the $VO_4$ motif of bulk $BiVO_4$ is maintained at this vacuum interface, and since no mid-gap states are formed, no substantial detriments to PEC performance would be expected in this vacuum termination. While the $BiVO_4$ layer at the vacuum interface in Fig. 6a is constrained to the bulk lattice parameters, we show in Fig. S3† that similar results are obtained with a fully-relaxed vacuum/$BiVO_4$ interface.

For comparison, we model a defective, uncoated $BiVO_4$ interface by introducing an O vacancy at the $BiVO_4$(010) surface. We note that this surface is appropriate for model studies as it is the lowest-energy surface of monoclinic $BiVO_4$ (ref. 45) and each surface O has the same coordination to Bi and V. In our calculations, a single O vacancy was introduced in a 2 × 2 supercell with 8 monolayers of $BiVO_4$, which corresponds to a 12.5% O deficiency on the O-terminated surface. The O vacancy initially causes a single V to be 3-fold coordinated by O in the model cell. As shown in Fig. 6b, subsequent relaxation of the supercell results in the V atom shifting by 0.4 Å out of the surface Bi–V plane to form a bond with an O atom in the underlying layer. The PDOS in Fig. 6b reveals that the O defect results in the formation of spin-polarized trap states that are occupied. The density of the mid-gap states is larger in the second layer than in the top layer due to the intra-layer V–O bond, and these near-surface states can trap photo-exited holes and cause Fermi level pinning.[46] Comparing Fig. 6a and b reveals the important role the $CeO_2$ coating plays in preserving O stoichiometry and in particular the integrity of the $VO_4$ structural units, mitigating recombination pathways at the $BiVO_4$ surface.

To further understand the electronic structure of our model heteroepitaxial interface, we create a supercell without vacuum/$BiVO_4$ interfaces by applying 2-monolayer $CeO_2$ terminations on both ends of an 8-layer $BiVO_4$ slab. The 2 central $BiVO_4$ monolayers are constrained to bulk $BiVO_4$ lattice parameters, allowing the remainder of the structure to be fully relaxed. The resulting cell is shown along with its band structure and element-projected DOS in Fig. 7. In the band structure of Fig. 7b, the eigenenergies at each $k$ point are colored by the contribution from the $BiVO_4$ or $CeO_2$ layers, providing additional insight into the electronic structure at the interface. While the eigenstates in the valence band each have different fractional contributions from the $BiVO_4$ and $CeO_2$ layers, the valence band structure is largely the same between the light absorber material and the metal oxide coating, which is desirable for efficient hole transport and results from the strong O 2p

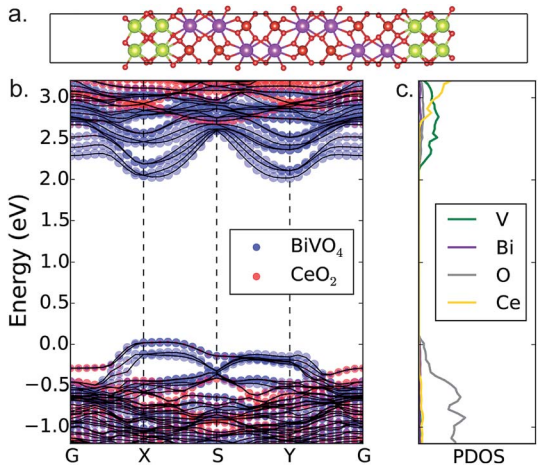


Fig. 7 (a) The $CeO_2$(001)/$BiVO_4$(010)/$CeO_2$(001) model system used to calculate the (b) in-plane band structure and (c) element-specific DOS of the heteroepitaxial system. The points in the band diagram correspond to the eigenenergies at the *k* points, and the blue and red dot sizes indicate the fractional contribution to the state fraction from $BiVO_4$ and $CeO_2$, respectively. The DOS diagram shows that O provides the most contribution to the valence band and that V and Ce provide the most contributions to the conduction band in the respective layers of the system. The VBM is set to 0 eV.

character in the valence band of both materials. The Ce-based conduction band in the overlayers is at much higher energy than the $BiVO_4$ conduction band.

While it is unlikely that the specific $CeO_2$(001)/$BiVO_4$(010) heteroepitaxial interface studied here is formed at a majority of the $BiVO_4$ crystal grains in our experimental electrodes, these calculations, summarized in Fig. 5–7, show how $CeO_2$ can improve the surface electronics of $BiVO_4$ photoanodes. While so-called "protective coatings" typically refer to protection against corrosion, our results highlight the importance of maintaining the integrity of the $VO_4$ units at the surface, which motivates exploration into whether the reported FeOOH coatings[13,18,19] also serve this purpose. While Fig. 3 demonstrates the importance of including Fe in the (Fe–Ce)-based coatings, Ce-rich coatings containing La and Co also perform well,[16] suggesting that the role of Fe may differ from that of pure FeOOH coatings and may involve enhancement of the coating conductivity or catalytic activity. Building model cells with either FeOOH/$BiVO_4$ interfaces or mixed Fe–Ce coatings does not appear to be straightforward, particularly due to the different structure, O-coordination and average metal oxidation state of FeOOH compared to $BiVO_4$. Indeed, $CeO_2$ is a particularly suitable coating for $BiVO_4$ due to its oxygen stoichiometry and approximate lattice match, which enables stabilization of the interfacial O layer to prevent defects such as that modelled in Fig. 6b.

As indicated by the Pourbaix diagram and observed in previous studies of Ce-rich electrocatalysts,[40] $Ce^{4+}$ is indeed expected to be the stable species under OER conditions. Interestingly, recent work on $Ce^{3+}$ alloying onto $Bi^{3+}$ sites in $BiVO_4$ indicates that $Ce^{3+}$ may improve particulate $BiVO_4$ photocatalysis due to the formation of a mid-gap Ce 4f state at energy slightly higher than the VBM of $BiVO_4$, which photo-excited holes can occupy to mitigate recombination.[47] Such hole-trapping phenomena are not necessarily beneficial in PEC processes since the ultimate goal is to transport the photo-generated holes to the catalytic surface as efficiently as possible. In our previous and present work we have demonstrated the beneficial effects of Ce-based coatings using both IJ and PVD deposition techniques, both of which could in principle lead to $Ce^{3+}$ doping of the $BiVO_4$ during deposition, while more detailed characterization is required to determine the composition and structure of the metal oxide/$BiVO_4$ interfaces. It is also worth noting that a detailed theoretical assessment of $IrO_2$/$WO_3$ photoanodes was recently reported by Ping *et al.*[20] in which the conformality of the coating played a critical role in interface energetics. While our IJ and PVD experimental results suggest that the (Fe–Ce)$O_x$/$BiVO_4$ is not highly sensitive to surface morphology, more detailed studies are required to determine if morphology optimization can provide additional improvement of PEC performance.

## Conclusions

By using combinatorial sputter deposition, optimal metal oxide coatings for $BiVO_4$-based OER photoelectrocatalysis are identified in a well-defined range of composition and loading centered at $Fe_{0.26}Ce_{0.74}O_z$ and 0.9 nmol $mm^{-2}$. The mixed-metal oxide coatings are quite uniform with roughness on the 10 nm-scale and excellent photoelectrochemical power generation is obtained with up to 90% Ce. A newly-identified heteroepitaxial $CeO_2$(001)/$BiVO_4$(010) interface provides a useful model system for revealing the impact of Ce in improving the surface structure and electronics of $BiVO_4$. $CeO_2$ facilitates the removal of surface states and enables efficient hole extraction from $BiVO_4$ while mitigating recombination. These findings identify $CeO_2$ as a highly beneficial material for developing coatings that enhance the photoelectrochemical properties of $BiVO_4$, motivating fundamental and engineering studies of $CeO_2$-rich coatings to further enhance photoelectrocatalysis of the OER for efficient solar fuel generation.

## Acknowledgements

This material is based upon work performed by the Joint Center for Artificial Photosynthesis, a DOE Energy Innovation Hub, supported through the Office of Science of the U.S. Department of Energy (Award No. DE-SC0004993). A. Shinde, G. Li and L. Zhou contributed equally to this work. The authors thank Ian Sharp for insightful discussions and Xinghao Zhou for assistance with AFM experiments.

## References

1 F. E. Osterloh and B. A. Parkinson, *MRS Bull.*, 2011, **36**, 17–22.
2 N. Guijarro, M. S. Prevot and K. Sivula, *Phys. Chem. Chem. Phys.*, 2015, **17**, 15655–15674.
3 K. Sivula and R. van de Krol, *Nat. Rev. Mater.*, 2016, **1**, 15010.

 

4 M. G. Walter, E. L. Warren, J. R. McKone, S. W. Boettcher, Q. Mi, E. A. Santori and N. S. Lewis, *Chem. Rev.*, 2010, **110**, 6446–6473.
5 J. K. Cooper, S. Gul, F. M. Toma, L. Chen, Y.-S. Liu, J. Guo, J. W. Ager, J. Yano and I. D. Sharp, *J. Phys. Chem. C*, 2015, **119**, 2969–2974.
6 F. M. Toma, J. K. Cooper, V. Kunzelmann, M. T. McDowell, J. Yu, D. M. Larson, N. J. Borys, C. Abelyan, J. W. Beeman, K. M. Yu, J. Yang, L. Chen, M. R. Shaner, J. Spurgeon, F. A. Houle, K. A. Persson and I. D. Sharp, *Nat. Commun.*, 2016, **7**, 12012.
7 K. Sayama, A. Nomura, Z. Zou, R. Abe, Y. Abe and H. Arakawa, *Chem. Commun.*, 2003, 2908–2909, DOI: 10.1039/b310428a.
8 F. F. Abdi, L. Han, A. H. M. Smets, M. Zeman, B. Dam and R. van de Krol, *Nat. Commun.*, 2013, **4**, 2195.
9 W. Luo, Z. Yang, Z. Li, J. Zhang, J. Liu, Z. Zhao, Z. Wang, S. Yan, T. Yu and Z. Zou, *Energy Environ. Sci.*, 2011, **4**, 4046–4051.
10 C. C. L. McCrory, S. Jung, J. C. Peters and T. F. Jaramillo, *J. Am. Chem. Soc.*, 2013, **135**, 16977–16987.
11 J. A. Haber, Y. Cai, S. Jung, C. Xiang, S. Mitrovic, J. Jin, A. T. Bell and J. M. Gregoire, *Energy Environ. Sci.*, 2014, **7**, 682–688.
12 W. A. Smith, I. D. Sharp, N. C. Strandwitz and J. Bisquert, *Energy Environ. Sci.*, 2015, **8**, 2851–2862.
13 J. A. Seabold and K.-S. Choi, *J. Am. Chem. Soc.*, 2012, **134**, 2186–2192.
14 H. Ye, H. S. Park and A. J. Bard, *J. Phys. Chem. C*, 2011, **115**, 12464–12470.
15 R. Saito, Y. Miseki, W. Nini and K. Sayama, *ACS Comb. Sci.*, 2015, **17**, 592–599.
16 D. Guevarra, A. Shinde, S. K. Suram, I. D. Sharp, F. M. Toma, J. A. Haber and J. M. Gregoire, *Energy Environ. Sci.*, 2016, **9**, 565–580.
17 A. Shinde, D. Guevarra, G. Liu, I. D. Sharp, F. M. Toma, J. M. Gregoire and J. A. Haber, *ACS Appl. Mater. Interfaces*, 2016, DOI: 10.1021/acsami.6b06714.
18 L. Chen, F. M. Toma, J. K. Cooper, A. Lyon, Y. Lin, I. D. Sharp and J. W. Ager, *ChemSusChem*, 2015, **8**, 1066–1071.
19 J. A. Seabold, K. Zhu and N. R. Neale, *Phys. Chem. Chem. Phys.*, 2014, **16**, 1121–1131.
20 Y. Ping, W. A. Goddard and G. A. Galli, *J. Am. Chem. Soc.*, 2015, **137**, 5264–5267.
21 Y. Park, D. Kang and K.-S. Choi, *Phys. Chem. Chem. Phys.*, 2014, **16**, 1238–1246.
22 T. W. Kim and K.-S. Choi, *Science*, 2014, **343**, 990–994.
23 T. H. Jeon, W. Choi and H. Park, *Phys. Chem. Chem. Phys.*, 2011, **13**, 21392–21401.
24 S. K. Suram, L. Zhou, N. Becerra-Stasiewicz, K. Kan, R. J. R. Jones, B. M. Kendrick and J. M. Gregoire, *Rev. Sci. Instrum.*, 2015, **86**, 033904.
25 R. H. Coridan, A. C. Nielander, S. A. Francis, M. T. McDowell, V. Dix, S. M. Chatman and N. S. Lewis, *Energy Environ. Sci.*, 2015, **8**, 2886–2901.
26 G. Kresse and J. Hafner, *Phys. Rev. B: Condens. Matter Mater. Phys.*, 1993, **47**, 558.
27 G. Kresse and J. Furthmuller, *Phys. Rev. B: Condens. Matter Mater. Phys.*, 1996, **54**, 11169.
28 J. P. Perdew, K. Burke and M. Ernzerhof, *Phys. Rev. Lett.*, 1997, **78**, 1396.
29 J. P. Perdew, K. Burke and M. Ernzerhof, *Phys. Rev. Lett.*, 1996, **77**, 3865.
30 V. I. Anisimov, J. Zaanen and O. K. Andersen, *Phys. Rev. B: Condens. Matter Mater. Phys.*, 1991, **44**, 943–954.
31 B. Himmetoglu, A. Floris, S. de Gironcoli and M. Cococcioni, *Int. J. Quantum Chem.*, 2014, **114**, 14–49.
32 I. A. Vladimir, F. Aryasetiawan and A. I. Lichtenstein, *J. Phys.: Condens. Matter*, 1997, **9**, 767.
33 A. I. Liechtenstein, V. I. Anisimov and J. Zaanen, *Phys. Rev. B: Condens. Matter Mater. Phys.*, 1995, **52**, R5467–R5470.
34 G. Kresse and D. Joubert, *Phys. Rev. B: Condens. Matter Mater. Phys.*, 1999, **59**, 1758.
35 P. E. Blochl, *Phys. Rev. B: Condens. Matter Mater. Phys.*, 1994, **50**, 17953.
36 M. B. Kanoun, A. H. Reshak, N. Kanoun-Bouayed and S. Goumri-Said, *J. Magn. Magn. Mater.*, 2012, **324**, 1397–1405.
37 J. Neugebauer and M. Scheffler, *Phys. Rev. B: Condens. Matter Mater. Phys.*, 1992, **46**, 16067.
38 G. Makov and M. C. Payne, *Phys. Rev. B: Condens. Matter Mater. Phys.*, 1995, **51**, 4014.
39 L. Trotochaud, T. J. Mills and S. W. Boettcher, *J. Phys. Chem. Lett.*, 2013, **4**, 931–935.
40 J. A. Haber, E. Anzenburg, J. Yano, C. Kisielowski and J. M. Gregoire, *Adv. Energy Mater.*, 2015, **5**, 1402307.
41 G. Pacchioni, *ChemPhysChem*, 2003, **4**, 1041–1047.
42 A. W. Sleight, H. Y. Chen, A. Ferretti and D. E. Cox, *Mater. Res. Bull.*, 1979, **14**, 1571–1581.
43 E. A. Kümmerle and G. Heger, *J. Solid State Chem.*, 1999, **147**, 485–500.
44 J. K. Cooper, S. Gul, F. M. Toma, L. Chen, P.-A. Glans, J. Guo, J. W. Ager, J. Yano and I. D. Sharp, *Chem. Mater.*, 2014, **26**, 5365–5373.
45 T. Liu, X. Zhou, M. Dupuis and C. Li, *Phys. Chem. Chem. Phys.*, 2015, **17**, 23503–23510.
46 H.-J. Lewerenz and L. Peter, *Photoelectrochemical Water Splitting*, The Royal Society of Chemistry, 2013.
47 Z. Y. Jiang, Y. Y. Liu, T. Jing, B. B. Huang, X. Y. Zhang, X. Y. Qin, Y. Dai and M. H. Whangbo, *J. Phys. Chem. C*, 2016, **120**, 2058–2063.